



## Full Length Article

## Development of the scintillating fiber timing detector for the Mu3E experiment

A. Bravar<sup>a,\*</sup>, A. Buonauro<sup>b</sup>, S. Corrodi<sup>c</sup>, A. Damyanova<sup>a</sup>, Y. Demets<sup>a</sup>, L. Gerritzen<sup>c</sup>, C. Grab<sup>c</sup>, C. Martin Perez<sup>c</sup>, A. Papa<sup>d</sup><sup>a</sup> Département de physique nucléaire et corpusculaire, Université de Genève, 24, quai Ernest-Ansermet, 1211 Genève 4, Switzerland<sup>b</sup> Physik-Institut, Universität Zürich, Winterthurerstrasse 190, 8057 Zurich, Switzerland<sup>c</sup> Institute for Particle Physics and Astrophysics, Eidgenössische Technische Hochschule, Otto-Stern-Weg 5, 8093 Zürich, Switzerland<sup>d</sup> Laboratory for Particle Physics, Paul Scherrer Institut, Forschungsstrasse 111, 5232 Villigen, Switzerland

## ARTICLE INFO

Dataset link: <https://doi.org/10.16907/10be2b23-4783-4c5e-a17f-7ffdf4eb6527>

## Keywords:

Tracker

Scintillating fibers

Silicon photo-multipliers

Timing

## ABSTRACT

We present the development and discuss the performance of a compact scintillating fiber detector for the Mu3E experiment for accurate time measurements at very high particle rates. Mu3E is a new experiment under preparation at the Paul Scherrer Institut (PSI) to search for charged Lepton Flavor Violation in the neutrinoless muon decay  $\mu^+ \rightarrow e^+ e^- e^+$  with a projected sensitivity of  $10^{-16}$  using the most intense continuous surface muon beam in the world.

A very thin scintillating fiber detector (thickness  $< 0.2\%$  of a radiation length  $X_0$ ) with a time resolution of about 250 ps, efficiency around 97%, and spatial resolution of  $\sim 100 \mu\text{m}$  has been developed. The SciFi detector is read out with multi-channel silicon photomultiplier arrays at both ends to achieve the best timing performance. Different scintillating fiber types have been evaluated and various assembly procedures have been tested to achieve the best performance.

## 1. Introduction

The Mu3E experiment [1] will search for charged Lepton Flavor Violation in the neutrinoless muon decay  $\mu^+ \rightarrow e^+ e^- e^+$  with the ultimate goal to find or exclude this process, if it occurs more than once in  $10^{16}$  muon decays. Since this process is heavily suppressed in the Standard Model with a branching ratio  $< 10^{-54}$ , any observation above this level will be a sign for new physics. Mu3E has the potential of probing for new physics at the PeV scale. The experiment is in preparation at the Paul Scherrer Institute (PSI) in Villigen and will use the most intense continuous surface muon beam in the world (currently  $\sim 1 \cdot 10^8$  muons/s). The Mu3E detector is based on high-voltage monolithic active silicon pixel sensors (HV-MAPS) for precise tracking in conjunction with scintillating fibers and scintillating tiles coupled to silicon photomultipliers for accurate timing measurements. Fig. 1 illustrates the cylindrical arrangement of the Mu3E sub-detectors around the muon stopping target, parallel to the beam. A detailed description of the Mu3E apparatus can be found in the Technical Design of the experiment [2].

The role of the timing detectors is to attach a time stamp to the tracks reconstructed in the silicon pixel detectors in order to suppress all forms of accidental backgrounds. For this purpose, a very thin

scintillating fiber (SciFi) detector with a thickness  $< 0.2\%$  of a radiation length  $X_0$  has been developed. The SciFi detector is read out at both ends with multi-channel silicon photomultiplier (SiPM) arrays [3], which will detect  $\mathcal{O}(15)$  photons per minimum ionizing particle (MIP) crossing. Acquiring the signals on both sides improves the time resolution and increases the detection efficiency of the whole system, because noise hits can be readily rejected. By taking the mean-time of the two time measurements, the time measurement is independent of the hit position (Fig. 28) and no position dependent correction is necessary. The SciFi detector will also help to reduce ambiguities in the track reconstruction and will reliably determine the sense of rotation (i.e. the charge) of the recurling tracks in the central region of the apparatus using the time of flight between consecutive crossings of the detector.

An overview of the state-of-the-art of scintillating fiber detectors before year 2000 can be found e.g. in [4]. The advent of SiPMs, in particular of multi-channel SiPM arrays pioneered by the PEBS experiment [5] and thoroughly studied in [6], has rekindled the interest in the SciFi technology and has led to the development of very large SciFi detectors, like the LHCb SciFi tracker [7].

The Mu3E SciFi detector is cylindrical in shape with a radius of 61 mm and a length of 300 mm (270 mm in the acceptance region). It

\* Corresponding author.

E-mail address: [alessandro.bravar@unige.ch](mailto:alessandro.bravar@unige.ch) (A. Bravar).

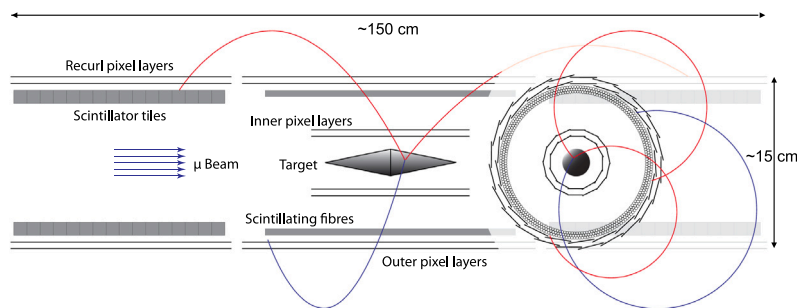


**Fig. 1.** Schematic view of the Mu3E apparatus in the side and transverse projections (not to scale) [2]. The Phase I setup consists of a central part and recurl stations up- and down-stream. The central part comprises, from inside out, a hollow double cone muon stopping target, a silicon pixel inner double layer, the SciFi's, and a second silicon pixel outer double layer. The apparatus is inserted in a 2.7 m long solenoid providing a 1 T homogeneous magnetic field.



**Fig. 2.** Full size SciFi ribbon prototypes. The fibers are assembled with different adhesives (the black epoxy gives the black color to the ribbons).

is composed of 12 SciFi ribbons longitudinally staggered by 10 mm to minimize gaps between the ribbons and to allow for the spring loading of the detector. The SiPM arrays will be read out with a dedicated mixed mode ASIC, the MuTriG [8], especially developed for Mu3E. The space constraints in the central part of the Mu3E apparatus impose a very compact design.

In the following we present the assembly of the SciFi ribbons and their physical properties, and the photo-sensors used for detecting the scintillation light. Then, we discuss the performance of the detector in terms of light yield, achievable time resolution, detection efficiency, etc. Different scintillating fiber materials and assembly procedures (i.e. the number of staggered SciFi layers) have been evaluated to achieve the best performance.

## 2. The scintillating fiber ribbons

In the Mu3E baseline design, the SciFi ribbons are formed by staggering 3 layers of 250  $\mu\text{m}$  diameter round high purity double-clad scintillating fibers from Kuraray [9], type SCSF-78MJ. The length of the fiber ribbons is 300 mm with a width of 32.5 mm. POLYTEC EP 601-BLACK epoxy is used for the assembly of the ribbons. This adhesive was chosen for its handling properties. The use of a  $\text{TiO}_2$  loaded adhesive is not a viable option due to the high  $Z$  of titanium, which would generate an unacceptably large amount of multiple scattering.<sup>1</sup> Fig. 2 shows several full size SciFi ribbons.

SciFi ribbons made with different blue-emitting fibers (Kuraray fibers SCSF-78 and SCSF-81 [9], Kuraray NOL-11 fibers [10], and Bicon BCF-12 fibers [11]) have been studied intensively in test beams. The timing characteristics of these fibers are discussed in [12], and their physical properties are summarized, for instance, in Table 1 of [12]. Only results for the high yield fibers SCSF-78 and NOL-11 are presented (the performance of the low light yield fibers SCSF-81 and BCF-12 is significantly worse and is not discussed). Novel NOL fibers, based on Nanostructured Organosilicon Luminophores [10], which have a very

short decay time of 1.1 ns, give the best timing performance. These fibers, however, were not available in sufficiently large quantities at the time of the construction of the SciFi detector.

### 2.1. Making of the scintillating fiber ribbons

With the help of the custom winding tool depicted in Fig. 3 (left), which includes two almost straight sections, the fibers have been assembled into ribbons consisting of 2 to 6 staggered fiber layers. The ribbons are formed layer-by-layer. To start, the U-channel (Fig. 3 right), made of PTFE, is tightly filled with a first layer of fibers. To ease the extraction of the ribbons, the U-channel is coated with a thin layer of wax-based spray, the Trennspray P6. The tight filling of the U-channel ensures a good alignment of the fibers, better than 10  $\mu\text{m}$  (Fig. 5), which is essential for good position resolution. No template to position the fibers nor support structure is used. Then, a thin layer of glue is applied. The amount of glue is minimized to reduce the amount of non-active materials. Before the glue completely dries, a second SciFi layer is added. The bottom layer helps to stagger the second layer and determines the overall alignment of individual fibers. Iterating the procedure, up to 6 layers can be staggered. Two ribbons are manufactured at the same time. To minimize edge effects, mainly due to the low amount of glue applied in the manufacturing process, these ribbons are slightly wider than their final width. After removing the ribbons from the winding tool, the excess edge fibers are peeled off, down to the design width of 32.5 mm. The bottom layer consists of 128 fibers. Each ribbon is then placed in a jig, and the end pieces for coupling the ribbons to the SiPM arrays are glued at each ribbon's end. Finally the ribbons are cut to the nominal length of 300 mm, and diamond polished.

Three different types of adhesive have been evaluated. A first set of ribbons has been prepared with the POLYTEC EP 601 epoxy, which is a two-component, clear, low viscosity adhesive. The epoxy is cured at room temperature. A second set of ribbons has been prepared by admixing  $\text{TiO}_2$  powder, 20% by weight, to the clear epoxy. The last and final set of ribbons has been prepared using the POLYTEC EP 601-BLACK adhesive, which is also a two component, black-colored, low viscosity adhesive. The highest reduction of the optical cross-talk between fibers has been observed with this black-colored adhesive due to the increased absorption of internally non-reflected photons.

### 2.2. Fiber alignment

Fig. 4 shows the diamond polished cross section of a 4-layer SciFi ribbon prototype. The position of each fiber has been determined with a pattern recognition algorithm applied to this cut view. The fibers in a layer are spaced by  $\sim 255 \mu\text{m}$  center-to-center with good uniformity throughout the ribbon, as it can be assessed from Fig. 5 (left). The 255  $\mu\text{m}$  pitch is due to non-uniformities in the fiber's cross section, which compensate when aligning several fibers in the same layer. The

<sup>1</sup> The material budget of all Mu3E detectors has to be minimized to achieve the required momentum resolution of  $\Delta p_{\text{p.e.}} < 0.5 \text{ MeV}/c$ .

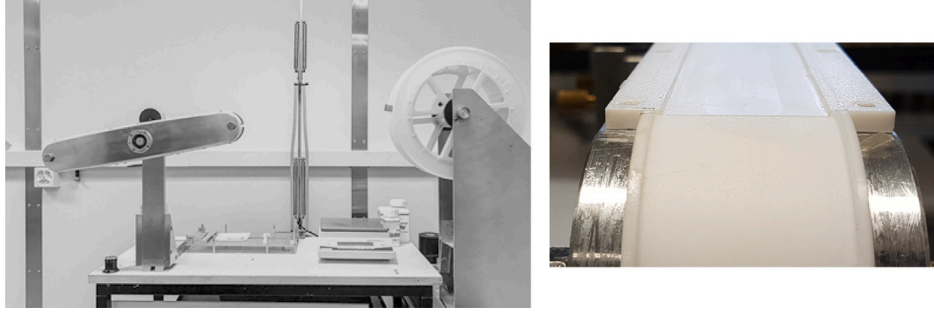


Fig. 3. (Left) Winding tool for the preparation of the 32.5 mm  $\times$  300 mm SciFi ribbons. Up to 6 SciFi layers can be staggered using this tool. (right) Detail of the U-channel.

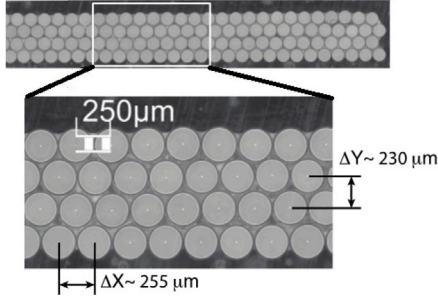


Fig. 4. Cut view of a diamond polished 4-layer SciFi ribbon. The cladding makes the fibers appear smaller in diameter. The centers of the fibers (white dots) are identified with a pattern recognition algorithm and their position is determined (Fig. 5).

separation between the layers is  $\sim 230 \mu\text{m}$  (Fig. 5 right), which gives an overall thickness of about  $710 \mu\text{m}$  for a 3-layer and  $940 \mu\text{m}$  for a 4-layer fiber ribbon. The thickness of a 3-layer SciFi ribbon, including the glue, corresponds to less than 0.2% of a radiation length  $X_0$ .

The mechanical integration of the SciFi detector in Mu3E is discussed in [2], where complementary information on the fiber ribbons can also be found.

### 3. The multi-channel silicon photomultiplier arrays

The SciFi detector is read out with the 128 channel Hamamatsu SiPM arrays, device S13552 [3], with a high quench resistance  $R_Q$ . This sensor has been developed for the LHCb experiment [7]. The large  $R_Q$  of  $\sim 500 \text{ k}\Omega$  allows to operate the SiPM arrays at high over bias voltages, and thus to increase the gain and the photon detection efficiency (PDE) of the sensor. The drawback is a longer decay time of the output signal and a longer recovery time. The sensor's segmentation is obtained by arranging the individual SiPM cells into independent readout columns or channels with a readout pitch of  $250 \mu\text{m}$ .

These sensors have been extensively studied by LHCb [13]. These sensors have a gain of  $3.8 \cdot 10^6$ , a peak PDE of 48% at 450 nm when operated at an overbias voltage  $V_{ob}$  of 3.5 V above the breakdown voltage  $V_{bd}$ . The dark count rate (DCR) of non-irradiated sensors at  $25^\circ\text{C}$  is  $\sim 15 \text{ kHz}$  per channel at a 0.5 photon equivalent threshold and  $\sim 0.5 \text{ kHz}$  at a 1.5 threshold. To characterize the sensors we measured the  $I - V$  curves for each channel of the SiPM arrays (see e.g. Figure 10.10 in [2]).  $V_{bd}$  (Fig. 6 left) and  $R_Q$  (Fig. 6 right) are determined channel by channel from the  $I - V$  measurements.  $V_{bd}$  varies within  $\pm 300 \text{ mV}$  of the central value for the same sensor, and varies from sensor to sensor within  $\pm 500 \text{ mV}$ , while  $R_Q$  is centered around  $500 \text{ k}\Omega$ . The repetitive pattern in  $V_{bd}$  comes from the fact that a single device consists of two separate dies. The alternating pattern in  $R_Q$  originates from the fact that the SiPM columns are bonded alternately on opposite sides of the sensor.

Fig. 8 shows a digitized pulse from one SiPM array channel. The shape of the pulse is characteristic of this SiPM: a fast rise time  $\tau_r < 1 \text{ ns}$  ( $\tau_r$  is limited by the speed of the amplifier) followed by a two-component decay with a sharp *kink* a few ns after the main peak. The short component has a decay time of  $\sim 1 \text{ ns}$ , while the decay time of the long component is  $\sim 50 \text{ ns}$ , which is due to the large  $R_Q$ . Our measurements are in good agreement with those of [13].

Since all channels share a common cathode, they are operated at the same bias voltage  $V_{bias}$ . This will lead to small gain differences between different channels, which can be compensated by adjusting  $V_{bias}$  for each channel individually. This is possible, for instance, with the MuTriG ASIC [8], which allows for the fine tuning of  $V_{bias}$  around a common value for each channel.

In Mu3E the photo-sensors will be operated at a temperature below  $-10^\circ\text{C}$  to reduce the DCR induced by the radiation damage. The irradiation of the sensors will be discussed in a separate work.

The fiber ribbons are coupled directly to the surface of the photo-sensors by mechanical pressure only provided by fixation screws with no optical interface. No one-to-one matching is possible between the fibers and the SiPM columns because of the staggering of the fibers (Fig. 13). The dead area between the SiPM columns adds an inefficiency of  $(1 - \epsilon_{fill-factor}) = 8\%$ , resulting in an overall PDE of 44%. A SiPM array with a smaller height could also be used, however we adopted this sensor, because at the time of procurement the thickness of the SciFi ribbons had not yet been fixed.

### 4. Test setup

The SciFi detector has been studied in extensive test beam campaigns at PSI in the  $\pi\text{M1}$  beamline. The beam was set at a momentum of  $210 \text{ MeV}/c$ . Beam particles were identified with time of flight measurements between the trigger cross of our setup (Fig. 7) and the RF signal of the proton cyclotron's accelerating cavities. The beam consisted of  $81\% \pi^+$ ,  $9\% \mu^+$ , and  $10\% e^+$ . For our studies we selected the most abundant particles, the pions. At this momentum the ionization energy loss of pions ( $\beta\gamma = 1.5$ ) is 20% higher than the energy that a MIP would deposit, and is comparable to the energy loss of highly relativistic particles, like the electrons from muon decays.

We assembled a telescope consisting of four SciFi modules, as illustrated in Fig. 7. All the detectors are placed in a light-tight box. Three out of four SciFi ribbons are used for tracking, while the third most downstream one is the device under test (DUT). The ribbons are mounted on motorized frames movable vertically for alignment and vertical scans. The DUT can also be tilted with respect to the beam around the horizontal axis, perpendicular to the beam, for angular scans. The whole setup is mounted on rails and can be moved transversely with respect to the beam for horizontal scans. A scintillator bar of  $125 \text{ mm} \times 12 \text{ mm} \times 6 \text{ mm}$  placed upstream and a scintillator cross formed by a horizontal bar of  $125 \text{ mm} \times 6 \text{ mm} \times 6 \text{ mm}$  and a vertical bar of  $85 \text{ mm} \times 10 \text{ mm} \times 6 \text{ mm}$  placed downstream are used for triggering on beam particles. These scintillators were coupled at both ends to Hamamatsu photomultipliers, model H6524. The trigger cross

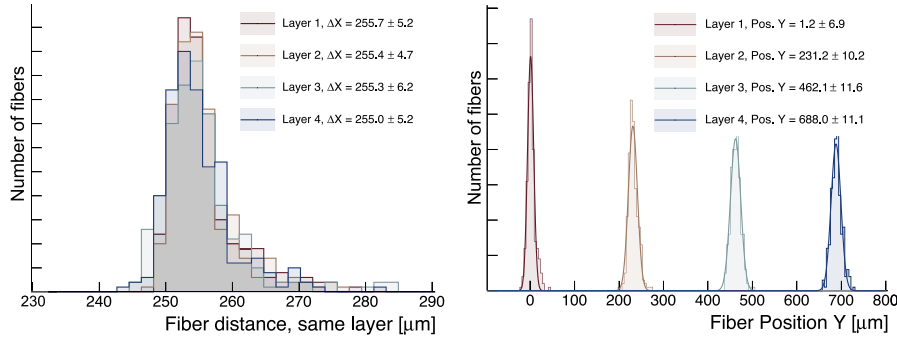


Fig. 5. Metrology of a 4-layer SciFi ribbon: (left) distance between neighboring fibers in the same layer, (right) vertical separation between the fiber layers.

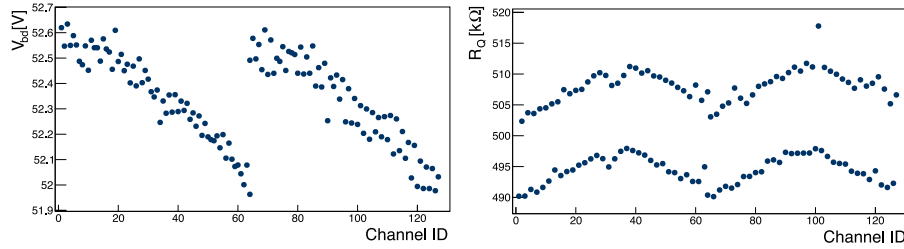


Fig. 6. Breakdown voltage  $V_{bd}$  (left) and quench resistance  $R_Q$  (right) determined from the  $I - V$  measurements for one SiPM array.

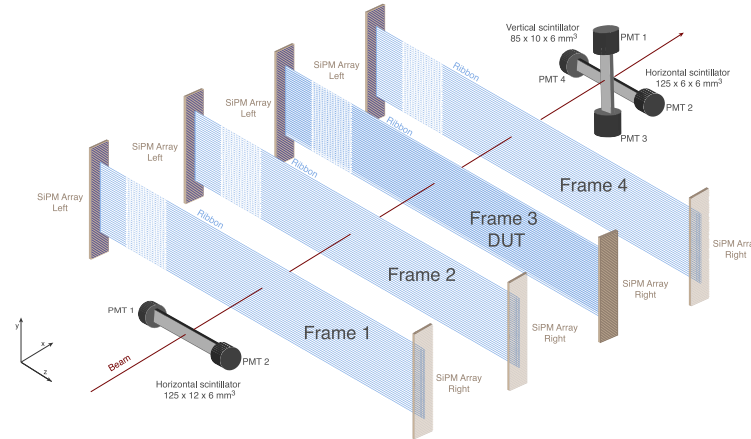


Fig. 7. Schematics of the SciFi telescope consisting of four SciFi ribbons and three trigger scintillators. The third most downstream detector is referred to as device under test (DUT).

also provided the external time reference for timing measurements with a time resolution of 80 ps. The acquisition of an event was triggered by a 3-fold coincidence between the 3 scintillator bars. The average continuous beam intensity was around  $10^6$  particles/s with a spot of  $15 \text{ mm} \times 10 \text{ mm}$  on the DUT (i.e. in the center of the telescope).

All SciFi ribbons are of the same manufacturing and size as the ones that will be used in Mu3E (i.e. 3 fiber layers, 300 mm long, and 32.5 mm wide). Not all the channels of the SiPM arrays, however, have been instrumented: 64 channels on each side of the DUT, corresponding to a vertical extension of 16 mm, and 32 channels on each side of the other SciFi modules, corresponding to a vertical extension of 8 mm, have been equipped with analog readout electronics based on fast transistor amplifiers providing single photo-electron amplitudes of  $\sim 100 \text{ mV}$ . The maximal amplified signal's amplitude did not exceed 1 V. The signals were recorded with 5 GHz waveform digitizers based on the DRS4 circular capacitor array [14]. Our digitizer boards comprise 32 analog input channels (i.e. four DRS4 ASICs) [15]. The readout of the SiPM arrays with the MuTriG ASIC will be discussed in a separate work.

## 5. Signal processing

Fig. 8 shows an example of waveforms recorded for one event. All information, like the charge and the arrival time of the scintillation photons, can be extracted from the waveforms. In this example, several consecutive channels show a large activity given that the light signal is spread over several columns of the SiPM array (Fig. 13). Most of the scintillation photons arrive at the same time and generate signals with steep rising edges. The starting time of the signal is determined by the trigger delay, which has been adjusted such to fully contain the pulses in the acquisition window. The shape of the pulses reflects the fact that not all scintillation photons are emitted at the same time.

To extract the charge generated by the scintillation photons in each SiPM channel, the waveforms are integrated over a time interval (i.e. gate) of 80 ns (400 samples). The baseline is evaluated on an event-by-event basis by averaging the waveform over 100 consecutive samples before the start of the signal (Fig. 8) and it is subtracted from the waveform event-by-event. Thanks to the single photon detection



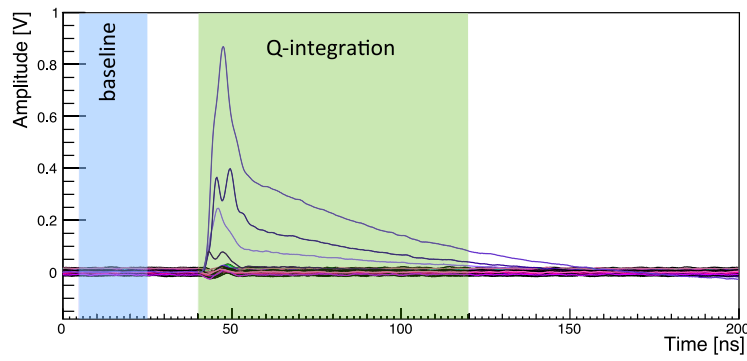


**Fig. 8.** Example of waveforms for 32 consecutive channels of the same SiPM array. Few adjacent SiPM channels (4 in this example) show a large activity (i.e. amplitudes  $> 100$  mV). Some electronic cross-talk at the level of 3% is visible in the non-active channels. The main part of the pulses is integrated over the “Q-integration” region to extract the charge, while the area labeled “baseline” is used for baseline evaluation.

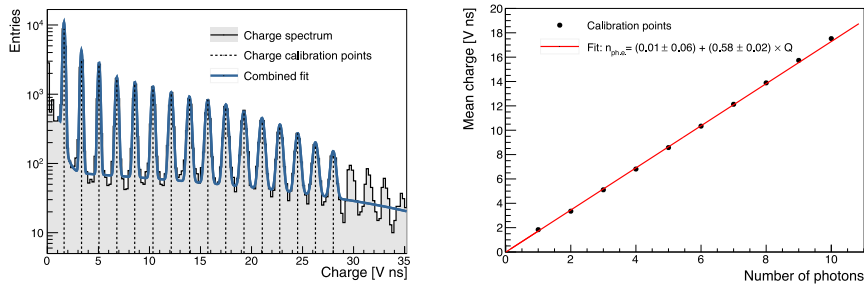


**Fig. 9.** (Left) Integrated charge distribution for one channel. Each peak corresponds to the number of detected photons in the event. (right) Correlation between the integrated charge and the number of detected photons.

capabilities of the SiPMs, the charge can be normalized to the charge generated by one photon without knowing the absolute amplification of the SiPM and of the readout electronics. Therefore, it can be expressed in terms of the number of detected photons or photo-electrons (ph.e.).

### 5.1. Charge normalization

The integrated charge distribution is shown in Fig. 9 (left) for one SiPM channel. Each peak above the *continuum*, coming mainly from the cross-talk between the SiPM cells in the same column, corresponds to a specific number of detected photons, and it is fitted with a Gaussian. The peak positions versus the corresponding number of photons  $n_{ph.e.}$  are displayed in Fig. 9 (right). The charge per detected photon is obtained by a linear interpolation, which at the same time validates the linear response of the sensor and of the readout electronics. In addition, the fit extrapolates to zero confirming the correct subtraction of the baseline. The gain of different channels shows an overall uniformity of 8%. The small variations are mainly due to differences in the gain of the SiPM array channels, which are operated at the same  $V_{bias}$ .

Fig. 10 shows the correlation between the normalized charge and the maximum signal amplitude for all active channels of the SiPM array. Some scintillation photons arrive later because of the de-excitation of the *spectral shifter*, and do not contribute to the build up of the leading edge of the signal, while they do add in the charge integral. This explains the spread of the amplitudes.

Hit selection is based on the signal's amplitude rather than the charge, since this information is readily available. This is also the operation mode of the MuTriG ASIC. To select a channel with a minimum number of detected photons  $n_{ph.e.}$ , thresholds are set between two consecutive peaks in the amplitude distribution (Fig. 11 left). The thresholds thus determined vary channel-to-channel within less than  $\pm 5\%$  for the same sensor. To better understand the impact of the thresholds on the normalized charge distribution (i.e. on  $n_{ph.e.}$ ) Fig. 11 (right) shows how these thresholds cut into the charge distribution: for instance, for a 1.5 ph.e. threshold about 5% of 1-photon events pass this

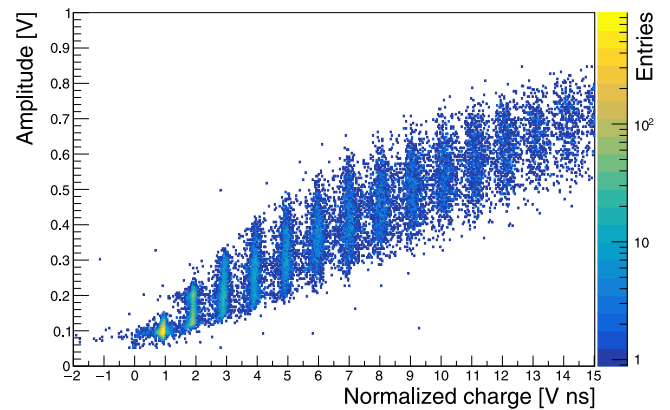


**Fig. 10.** Integrated charge (normalized to 1 ph.e.) vs maximum signal amplitude. A 0.25 ph.e. amplitude threshold has been applied to remove inactive channels.

selection, while about 20% of 2-photon events are lost. The threshold setting is particularly relevant for the detection efficiency of the SciFi detector.

### 5.2. Left-right correlations

Fig. 12 shows the correlation between *hits* detected in the two SiPM arrays at opposite ends of the SciFi ribbon for 0.5 ph.e. and 1.5 ph.e. thresholds. The extension of the correlation reflects the vertical extension of the beam spot impinging on the ribbon. From the width of the correlations one can estimate the spread of the optical signal over several channels of the SiPM array.

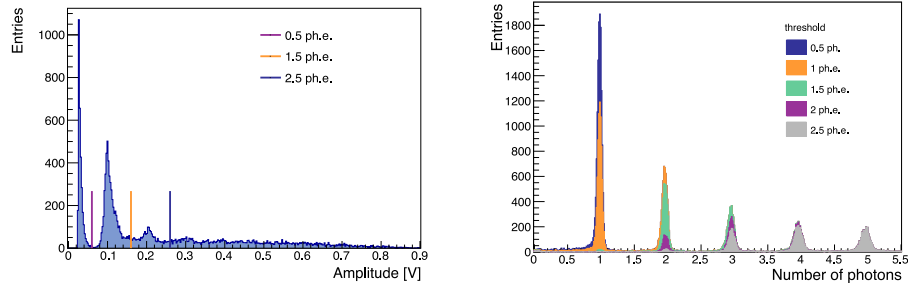


Fig. 11. (Left) Signal maximum amplitude for one selected channel. (right) Effect of the amplitude thresholds on the normalized charge distribution for the same channel.

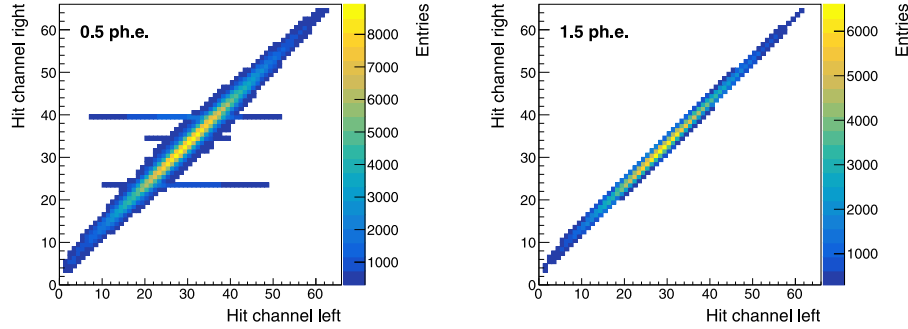


Fig. 12. Correlation between the hits generated in the two SiPM arrays at each side of a SciFi ribbon for a 0.5 ph.e (left) and 1.5 ph.e (right) threshold. Each column/row represents an individual 250  $\mu\text{m}$  SiPM channel. Some noise is visible at the 0.5 ph.e. threshold level.

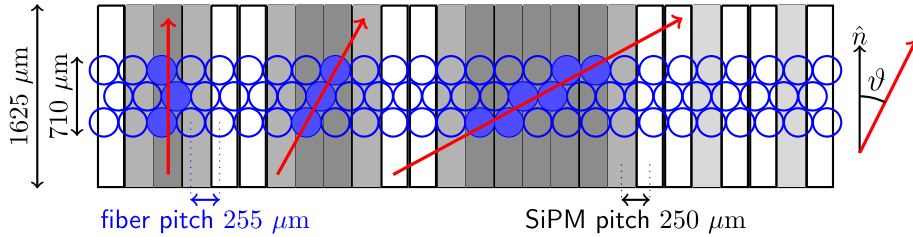


Fig. 13. Transverse view of a 3-layer SciFi ribbon mapped to a SiPM array. A particle crossing the ribbon excites some fibers (dark bullets), which can trigger avalanches in several channels of the SiPM array (dark gray). The optical cross-talk spreads the signal to neighboring channels (gray). The width of the cluster depends also on the particle's incident angle (left to right 0°, 30°, and 60°). Dark counts (light gray) should be excluded from the cluster.

## 6. Clustering

Because of the mapping of the fibers to the columns of the SiPM array, optical cross-talk between the fibers, delta rays, the photon's exit angle, light scattering at the optical junction between the SciFi ribbon and the photo-sensor, etc. the light signal is spread over several adjacent SiPM columns (Fig. 13). In  $\text{Mu3E}$  particles will cross the SciFi ribbons at large angles, which will spread the light signal even further.

The first step in forming a cluster is to select candidate SiPM channels, which fulfill the following constraints:

- the amplitude of the selected channels should pass a predefined threshold level of 0.5 ph.e. or higher (the same threshold is applied to all channels);
- the peak of the signal is matched to the trigger time within a  $-5$  ns and  $+10$  ns window (this requirement removes dark counts below the 0.2% level at a DCR of 15 kHz for a 0.5 ph.e. threshold).

Next, the selected channels are grouped in clusters:

- only directly contiguous channels are placed in a cluster (a one channel gap to account for dead channels is allowed);
- a minimum hit multiplicity, usually of two, is imposed on the cluster;

- the cluster must be matched to a track reconstructed in the SciFi telescope;
- finally, the cluster time is set to the earliest time stamp of the SiPM channels assigned to it, i.e. to the first detected photon.

### 6.1. Cluster width

The clusters thus reconstructed are shown in Fig. 14 for a 3-layer SCSF-78 fiber ribbon prepared with black epoxy<sup>2</sup> for 0.5 ph.e., 1.5 ph.e., and 2.5 ph.e. thresholds. Each ribbon end is shown separately. The vertical scale in the figure is normalized to the total number of analyzed events, i.e. the integral of the distribution is one. The zero-width entry corresponds to events in which no cluster has been found, and it is a first indication of detection inefficiency. As the threshold increases, the cluster width shrinks. Channels on the outskirts of the cluster are characterized by smaller signal amplitudes (lower  $n_{\text{ph.e.}}$ ), and are thus removed. From geometry consideration, on average, two consecutive SiPM columns are excited (Fig. 13), while broader clusters are observed. This is driven by the optical cross-talk between the

<sup>2</sup> In the following we will refer to ribbons prepared with black epoxy as *black* ribbons, and to those prepared with clear epoxy with an admixture of  $\text{TiO}_2$  as *clear* +  $\text{TiO}_2$  ribbons.

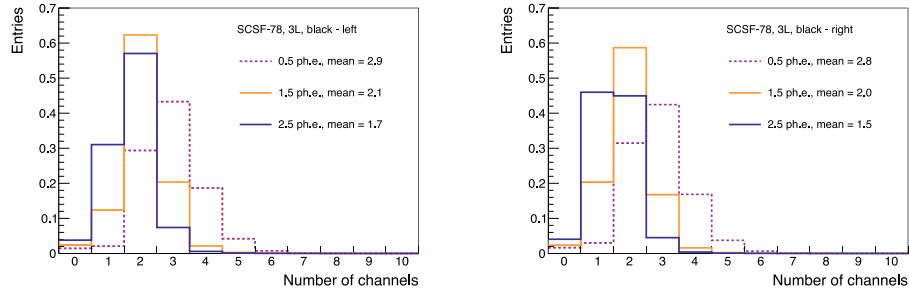


Fig. 14. Cluster width for particles crossing perpendicularly in the center a 3-layer SCSF-78 *black* fiber ribbon for 0.5 ph.e., 1.5 ph.e., and 2.5 ph.e. thresholds: (left) 15 cm from the left ribbon's end, (right) 15 cm from the right ribbon's end.

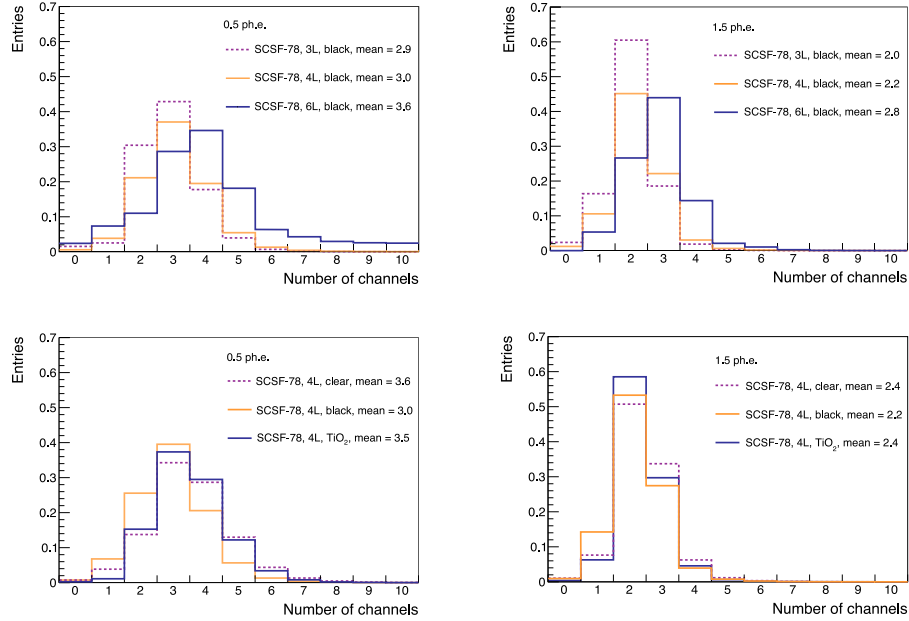


Fig. 15. Comparison of cluster widths for 0.5 ph.e. (left) and 1.5 ph.e. (right) thresholds for (top) 3-, 4- and 6-layer SCSF-78 *black* fiber ribbons, and (bottom) 4-layer SCSF-78 ribbons prepared with different adhesives (see legend).

fibers and at the photo-sensor optical junction. The cluster widths at both SciFi ribbon ends can also be compared in Fig. 14. The clusters widths are comparable at low thresholds. A difference, however, for the highest threshold of 2.5 ph.e. is observed. This can be explained by the alignment of the SciFi ribbon to the SiPM array, which was not the same for both ribbon ends.

The cluster widths for 3-, 4-, and 6-layer SciFi ribbons are compared in Fig. 15 (top). In this and the following figures the left side clusters are shown. The broadening of the clusters width of  $\sim 0.5$  channels observed for 6-layer SciFi ribbons is likely due to the higher light yield of these ribbons, which increases the probability of detecting photons at the outskirts of the cluster. Fig. 15 (bottom) compares the cluster widths for ribbons prepared with different adhesives (clear, black, and clear + 20%  $\text{TiO}_2$  admixture). The biggest reduction in the cluster width at the 0.5 ph.e. threshold, although of  $\sim 0.5$  channels only, is observed for the SciFi *black* ribbons. This implies also that the highest reduction of the optical cross-talk between fibers is obtained with black epoxy, because of a higher absorption of the non-reflected photons.

In  $\text{Mu3E}$ , positrons from muons decaying in the stopping target will cross the SciFi ribbons at angles ranging from  $10^\circ$  to  $90^\circ$  because of the bending in the magnetic field. The observed cluster width scales as  $1/\cos \theta$ , as expected from geometry considerations. To reduce the cluster width at large incident angles, one has to reduce the number of staggered fiber layers. This is one of the reasons for selecting 3-layer ribbons for  $\text{Mu3E}$ .

## 6.2. Cross-talk

Optical cross-talk between fibers is observed when scintillation photons originating from one fiber are trapped and propagate to the photo-sensor through another, usually neighboring fiber. To investigate in detail the optical cross-talk, specially prepared SciFi ribbons, in which each fiber is individually coupled to a single-channel SiPM, have been produced (Fig. 16). Two different SciFi ribbons have been prepared: one using clear epoxy, the second with a 20%  $\text{TiO}_2$  admixture in the epoxy. At the time when these measurements have been performed, the black epoxy has not yet been considered; it has not been possible to repeat these measurements later with the black epoxy.

The crossing point, after cluster identification, is set in the fiber with the largest signal amplitude (i.e. the seed fiber) in each fiber layer of the SciFi ribbon. A 0.5 ph.e. threshold has been applied to all SiPM channels. Fig. 17 shows the fraction of events in which photons have been detected in fibers adjacent to the seed fiber as a function of the distance from this fiber. Typically, one or two photons are detected in these fibers, and would not be counted at higher thresholds. The distribution is symmetric around the seed fiber. In absence of cross-talk, only one fiber would give a signal. Admixing  $\text{TiO}_2$  to the epoxy reduces the cross-talk between the fibers by about 50%.

## 7. Light yield

To determine the light yield of a SciFi ribbon we have to sum over all active channels of the SiPM array, since the light signal is

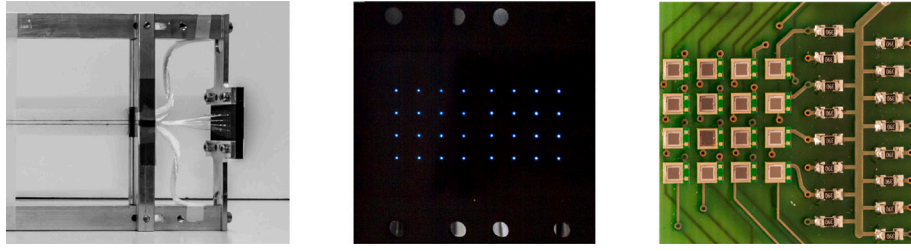


Fig. 16. Individual fiber readout: each fiber in the SciFi ribbon (left) is placed in a socket (middle) and coupled to a single channel SiPM (right).

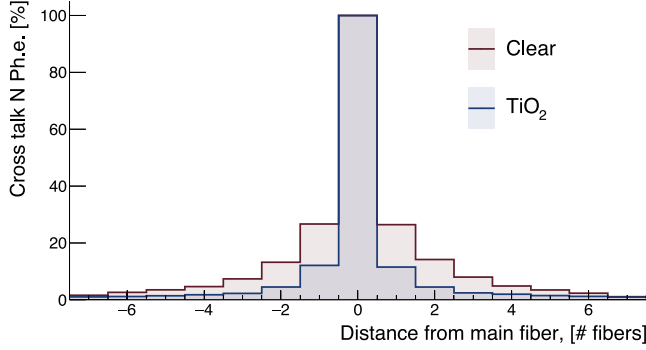


Fig. 17. Fraction of events in which scintillation photons have been detected in neighboring fibers in conjunction to the seed fiber (bin centered at 0) in the same layer.

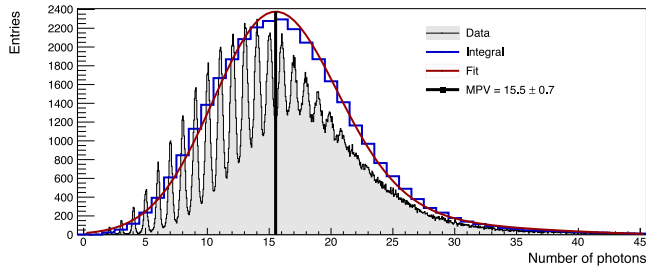


Fig. 18. Normalized cluster charge spectrum for a 3-layer SCSF-78 black fiber ribbon. Beam particles cross the SciFi ribbon in the center. The  $n_{\text{ph.e.}}$  distribution (histogram) is fitted with a convolution of a Gaussian and a Landau distribution and the MPV is extracted.

spread over several channels. The channel selection is the same as for the cluster formation, however, there is no minimum multiplicity requirement, i.e. the cluster can consist of only one channel. Fig. 18 shows the normalized charge spectrum summed over all active channels in the cluster for a 3-layer SCSF-78 black fiber ribbon. The peaks are evenly spaced up to high multiplicities confirming the linear response of the detector. To extract  $n_{\text{ph.e.}}$ , the normalized charge distribution has been integrated in a region of  $\pm 0.5$  around each peak. The discrete distribution  $n_{\text{ph.e.}}$  has then been fitted with a convolution of a Gaussian and a Landau distribution, which interpolates well the observed spectrum, and the Most Probable Value (MPV) of the convolution is extracted. In the following we will quote the MPV of the convolution as an estimate for the light yield of the SciFi ribbons  $\langle n_{\text{ph.e.}} \rangle$ .

Fig. 19 compares the light yield of SCSF-78 and NOL-11 fiber ribbons consisting of different numbers of staggered fiber layers, and assembled with different types of adhesives, as well. The MPV of the fits are also shown in the figure. These values are not corrected for the PDE of the SiPM array. A detailed study of the light yield of different blue-emitting scintillating fibers can be found e.g. in [12]. The light yield for the SCSF-78 and the NOL-11 fiber ribbons prepared with the same adhesive is comparable (Fig. 19 top left).

The light yield increases almost linearly with the number of staggered layers (Fig. 19 top right), and it is twice as large for a 6-layer fiber ribbon compared to a 3-layer ribbon. SciFi ribbons coated with  $\text{TiO}_2$  show a 15% higher light yield compared to black ribbons (Fig. 19 bottom left) due to the increased diffusion of scintillation photons at the fiber's surface. As the incident angle  $\vartheta$  increases, the thickness of the SciFi ribbon seen by the crossing particle increases as  $1/\cos \vartheta$ , and the light yield follows the same trend (Fig. 19 bottom right).

To evaluate the uniformity of the response, various SciFi ribbons have been scanned vertically (i.e. across the ribbon) and the light yields at the left and right sides have been compared. From Fig. 20, which shows an example of a vertical scan performed in the middle of NOL-11 fiber ribbons, it can be observed that indeed the light yield is quite uniform across the ribbons.

### 7.1. Light attenuation

To study the light attenuation, the SciFi ribbons have been scanned horizontally from 5 cm to 25 cm from the ribbon's end. The light intensity  $I$  as a function of the propagation distance  $d$  is usually described in terms of a short and a long attenuation component, which depends also on the scintillation light wavelength  $\lambda$ , as:

$$I(\lambda, d) = I_0^{\text{short}}(\lambda) \cdot \exp[-d/\Lambda^{\text{short}}(\lambda)] + I_0^{\text{long}}(\lambda) \cdot \exp[-d/\Lambda^{\text{long}}(\lambda)], \quad (1)$$

with  $\Lambda^{\text{short}}(\lambda)$  and  $\Lambda^{\text{long}}(\lambda)$  the attenuation lengths for the short and long components, respectively. At these lengths (i.e.  $\leq 30$  cm), the absorption of light is controlled by the short component  $\Lambda^{\text{short}}$ , which dies off rather quickly after 10 – 15 cm [12], while the long component can be assumed constant over the length of the SciFi ribbon.

Fig. 21 shows the number of detected photons  $\langle n_{\text{ph.e.}} \rangle$  as a function of the distance from the ribbon's ends for two different SciFi ribbons. The relatively small differences are due to the optical couplings of the fibers to the SiPM arrays, the PDE of each SiPM array, non-uniformities in the fibers, etc. The measurements are fitted with a single exponential function describing the short component  $\Lambda^{\text{short}}$ , while keeping the long component constant, since this component does not vary significantly over the length of our SciFi ribbons. The extracted attenuation lengths  $\Lambda^{\text{short}}$  range between 10 cm to 15 cm and are compatible within errors.

## 8. Timing analysis

The timing performance of the SciFi detector is the most important feature for the charge identification of the reconstructed tracks and background rejection in Mu3E. The intrinsic limit on the time resolution of low mass (i.e. thin) scintillation detectors is driven by the statistical processes involved in the generation of the light signal and fluctuations in the light detection. The time resolution of a relatively low light yield SciFi detector ( $\mathcal{O}(15)$  detected photons) depends on the decay time  $\tau$  of the spectral shifter (the shorter the decay time, the better the achievable time resolution), but also on the number of detected photons  $n_{\text{ph.e.}}$ . For a detailed discussion, see e.g. [12].

Fig. 22 shows the arrival time of the first detected photon in a selected channel of the SiPM array coupled to a 3-layer SCSF-78 black fiber ribbon. The shape of the arrival time distribution can be



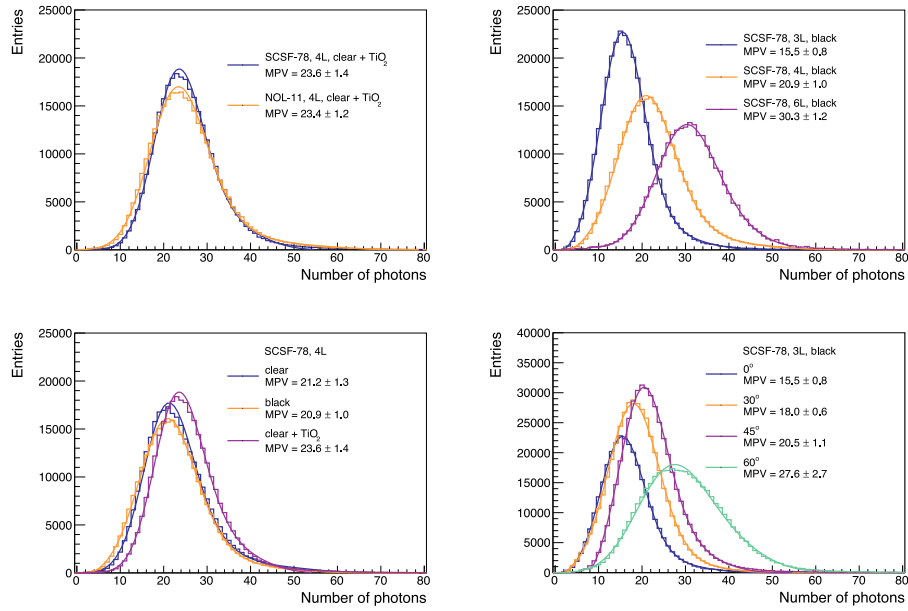


Fig. 19. Comparison of the light yield of different SciFi ribbons made with different fiber types, consisting of different numbers of staggered fiber layers, and assembled with different types of adhesives. Also compared are the light yields for different crossing angles. For the SciFi ribbon type and the crossing angle see the legends.

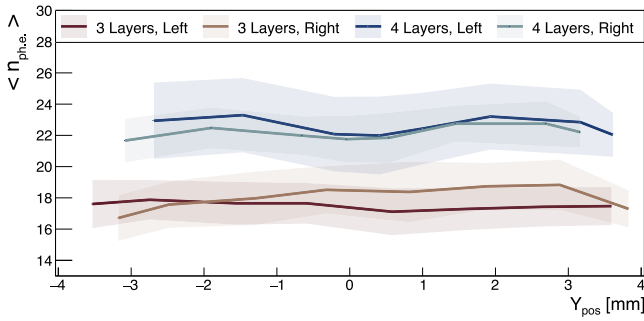


Fig. 20. Light yield across 3- and 4-layer NOL-11 ribbons measured always at the same distance of 15 cm from the photo-sensors. The light yields at the left and right ends of the ribbons are compared. Both ribbons have been assembled with clear epoxy + 20% TiO<sub>2</sub>.

described by a convolution of a Gaussian, which describes the time spread of the light pulse generation processes and fluctuations in the light detection, with an exponential decay function describing the de-excitation of the *spectral shifter*, the so called exponentially modified Gaussian distribution (EMG) or exGaussian:

$$F(t, \mu, \sigma, \tau) = A \frac{1}{2\tau} \exp \left[ \frac{\mu - t}{\tau} + \frac{\sigma^2}{2\tau^2} \right] * \left\{ 1 - \operatorname{erf} \left[ \frac{1}{\sqrt{2}} \left[ \frac{\mu - t}{\sigma} + \frac{\sigma}{\tau} \right] \right] \right\}, \quad (2)$$

where  $\tau$  is the scintillation light decay time and  $\sigma$  accounts for the time spread of the light generation and collection. erf is the error function,  $t = T_{\text{ch}} - T_{\text{trigger}}$ , and  $A$  is a normalization factor.

The arrival time of the first scintillation photon is extracted by interpolating the rising edge of the digitized pulses with a straight line extrapolated to the baseline of the waveform, after correcting for baseline fluctuations. The interpolation is performed on four consecutive samples on the rising edge: the first sample is below the single photon half amplitude, the next three samples are above. At 5 GHz sampling, the samples are spaced by 200 ps. The time walk of this algorithm has been estimated to be below 10 ps [12]. Incidentally, Fig. 22 also

gives an appreciation of the time resolution achievable with single-sided readout of the fiber detector, which is dominated by the decay time  $\tau$  of the *spectral shifter* at low photon statistics.

### 8.1. Time difference $\Delta T$

The time resolution of the SciFi detector can be significantly improved by reading out the detector at both ends and by combining both time measurements. That, however, requires time matched clusters at both SciFi ribbon's ends, which can reduce the detection efficiency of the detector.

Firstly, we have studied the time difference  $\Delta T = T_{\text{left}} - T_{\text{right}}$  distribution, where  $T_{\text{left}}$  and  $T_{\text{right}}$  are the time measurements for the *left* and *right* SciFi ribbon ends, respectively.  $\Delta T$  is self-contained in the sense that it can be formed without an external time reference, but it cannot be used to determine the crossing time of a particle. Fig. 23 shows the  $\Delta T$  distribution for a 3-layer SCSF-78 *black* fiber ribbon for beam particles crossing the SciFi ribbon in the center. The  $\Delta T$  distribution is symmetric around the peak, since the fluctuations in the time measurements subtract symmetrically for  $T_{\text{left}}$  and  $T_{\text{right}}$ . The tails, which extend symmetrically around the peak, are driven by the fiber's decay time. Several models have been used to describe the  $\Delta T$  distribution and to extract the time-difference resolution  $\sigma_{\Delta T}$ .

In the first approach, the  $\Delta T$  distribution is fitted with a Gaussian within  $\pm 4\sigma$  around the peak. The Gaussian describes reasonably well the core of the  $\Delta T$  distribution, however it fails to describe the tails. The fraction of events in the tails is below 10%.

Next, the  $\Delta T$  distribution is fitted with the sum of two Gaussian distributions centered around a common mean value. The first Gaussian, which describes the core of the distribution, can be interpreted as due to fluctuations in the excitation of the primary dies in the fibers (i.e. the *activator*) and in the light detection, while the second Gaussian describes the tails. In this example, more than 90% of events fall under the first Gaussian, while less than 10% under the second. In the following, we will use the sum of two Gaussians to describe the  $\Delta T$  distributions. As an indication of  $\sigma_{\Delta T}$  we quote the FWHM/2.35 of the  $\Delta T$  distribution, which is close to the width of the first Gaussian.

Alternatively, the  $\Delta T$  distribution can be modeled with a symmetric exponential function such as the Laplace distribution, which is a direct consequence of the Poissonian nature of the scintillation process,

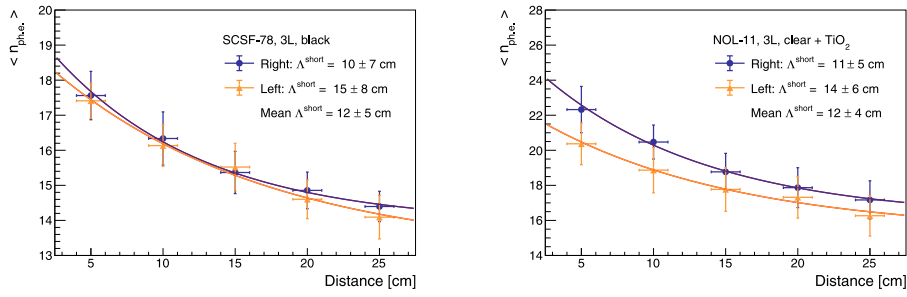


Fig. 21. Light yield  $\langle n_{\text{ph.e.}} \rangle$  as a function of the distance from both SciFi ribbon's ends for a 3-layers SCSF-78 black fiber ribbon (left) and a 3-layers NOL-11 clear + 20% TiO<sub>2</sub> fiber ribbon (right). The data points are fitted with a single exponential function.

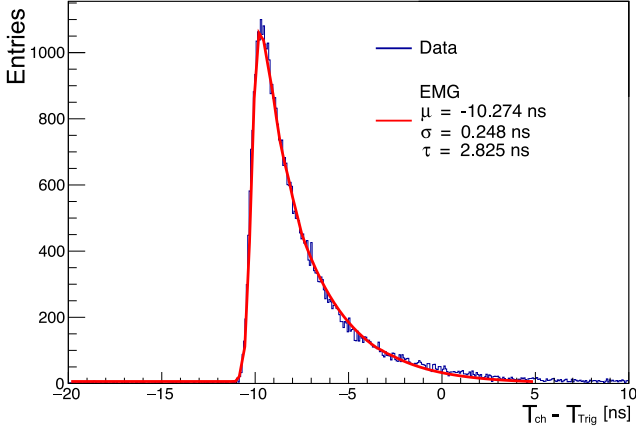


Fig. 22. Time of arrival of the first detected photon  $T_{\text{ch}} - T_{\text{trigger}}$  for a 3-layer SCSF-78 black fiber ribbon. The data is described by the exponentially modified Gaussian distribution with parameters  $\mu$ ,  $\sigma$  and  $\tau$ .

smearred with a Gaussian distribution to account for the time spread of the light collection. This convolution models rather well the  $\Delta T$  distribution, in particular the tails.

Fig. 24 compares the  $\Delta T$  distribution for 4-layer SCSF-78 and NOL-11 fiber ribbons. The timing performance of all measured SciFi ribbons is summarized in Table 1. The FWHM/2.35 of the  $\Delta T$  distributions ranges between 400 ps and 450 ps depending on the fiber type and the number of staggered fiber layers. The best  $\sigma_{\Delta T}$  resolution of 400 ps has been achieved with a 4-layer NOL-11 clear + TiO<sub>2</sub> fiber ribbon. Despite the significantly smaller decay time of the NOL-11 fiber of 1.1 ns, SciFi ribbons made with this fiber show a relatively small improvement with respect to the SCSF-78 fiber, which has a 2.8 ns decay time. That suggests that  $\sigma_{\Delta T}$  is dominated by the light yield, which is comparable for the two SciFi ribbon types (Fig. 19), and not by the decay time of the wavelength shifter.

## 8.2. Light propagation in the fibers

Fig. 25 shows the peak position of the  $\Delta T$  distribution for different beam impact points along the SciFi ribbon. The width of the  $\Delta T$  distributions along the ribbon remains almost constant, indicating that  $\sigma_{\Delta T}$  does not depend on the beam impact point. The data points can be interpolated with a straight line supporting the idea that the light propagates uniformly in both directions. Within our resolution, we do not observe edge effects as we approach the ends of the fiber ribbon. Taking into account that the difference in the traveled distance by the scintillation photons is twice the displacement, from the slope one can derive the speed of light propagation in the fibers  $v_{\text{fiber}} = 2 \times \Delta z / \Delta T$ . We find that the scintillation photons propagate at a speed which is roughly half the speed of light  $c$  in vacuum, i.e.  $v_{\text{fiber}} \sim 0.5 \times c$ .  $v_{\text{fiber}}$  is

significantly lower compared to the speed that one would expect from the refractive index  $n$  of the fiber, i.e.  $c/n$ . This can be understood by the fact that during propagation the photons are reflected internally from the cladding several times before reaching the photo-sensors and therefore travel a longer distance. From  $\Delta T$  one can also determine the particle's crossing point  $z$  along the fiber  $z = \frac{1}{2}L + \Delta T \times \frac{1}{2}v_{\text{fiber}}$  ( $L$  is the length of the fiber ribbon) with a resolution  $\sigma_z = \sigma_{\Delta T} \times \frac{1}{2}v_{\text{fiber}}$  of  $\sim 3$  cm (assuming  $\sigma_{\Delta T} = 400$  ps).

A dataset has also been collected in absence of ionizing particles to study the efficiency of the clustering algorithms in rejecting dark counts. When a SiPM cells discharges (dark count) it generates also infrared photons. Some IR photons escape from the SiPM and can be trapped and transported by the scintillating fibers to the opposite end, where they can trigger a discharge in the SiPM at this side. Fig. 26 (left) shows the correlation between hits at both ribbon's ends generated by random discharges in one of the SiPM arrays. A clear correlation emerges between the two sides proving that such events indeed occur. Fig. 26 (right) shows the time difference  $T_{\text{left}} - T_{\text{right}}$  for such events. The two peaks are separated by  $\sim 4.2$  ns, while the two events are separated by  $|\Delta T|$ , i.e.  $\sim 2.1$  ns. The speed of light propagation in the fibers from this measurement is therefore  $v_{\text{fiber}} = L/|\Delta T| = 30 \text{ cm} / 2.1 \text{ ns} \sim 0.5 \times c$ , which is in agreement with the above measurements.

## 8.3. Mean-time

The common approach to measure time, when reading out a scintillator at both ends, is to form the so called Mean-Time  $MT$ , defined as

$$MT = \frac{1}{2}(T_{\text{left}} + T_{\text{right}}) - T_0, \quad (3)$$

where  $T_0$  represents an external time reference, which could come from a low jitter trigger, or from a second timing measurement, like in a time-of-flight measurement, or from the system clock.  $T_0$  can be considered as an additive constant, provided that  $\sigma_{T_0}$  is small compared to the width of the  $MT$  distribution. For these studies,  $T_0$  is provided by the trigger time  $T_{\text{trigger}}$ .

By construction, one would expect that

$$\sigma_{MT} = \frac{1}{2}\sigma_{(T_{\text{left}}+T_{\text{right}})} = \frac{1}{2}\sigma_{(T_{\text{left}}-T_{\text{right}})} = \frac{1}{2}\sigma_{\Delta T}. \quad (4)$$

In general this assumption holds, provided that the time measurements are normally distributed, as would be the case with a thick scintillator ( $\mathcal{O}(100)$  detected photons). The  $MT$  distributions for 3-layer and 4-layer SCSF-78 SciFi black and NOL-11 clear + 20% TiO<sub>2</sub> ribbons are shown in Fig. 27. These measurements have been taken with the beam crossing the SciFi ribbons in the center. The  $MT$  distributions are not symmetric with respect to the peak and exhibit a tail extending to the right. The distributions are well described by the EMG distribution (Eq. (2)). More than 80% of events are described by the Gaussian. This is consistent with the shape of the  $\Delta T$  distributions (Fig. 23). Since the  $MT$  distributions are not too skewed, we take  $\sigma_{\text{core}}$  of the  $MT$  distribution as indication for the time resolution  $\sigma_{MT}$ . Otherwise we

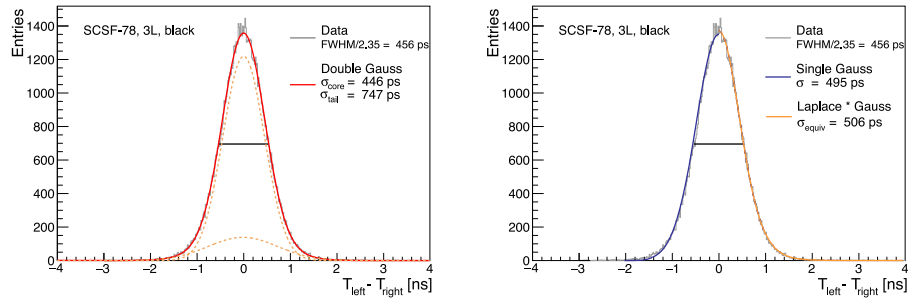


**Fig. 23.**  $\Delta T = T_{\text{left}} - T_{\text{right}}$  distribution for a 3-layer SCSF-78 SciFi *black* ribbon. The distribution is fitted with different models: (left) a double Gaussian distribution with a common mean; (right) a single Gaussian distribution, and an exponential distribution convoluted with a Gaussian. The latter two are fitted symmetrically around the peak, but are shown only on one side to enhance clarity. Also shown is the FWHM of the  $\Delta T$  distribution.

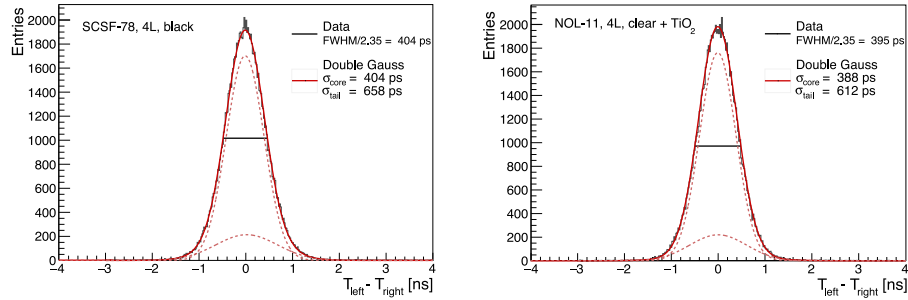


**Fig. 24.**  $\Delta T = T_{\text{left}} - T_{\text{right}}$  distribution for a 4-layer SCSF-78 *black* fiber ribbon (left) and a 4-layer NOL-11 *clear* + 20%  $\text{TiO}_2$  fiber ribbon (right).

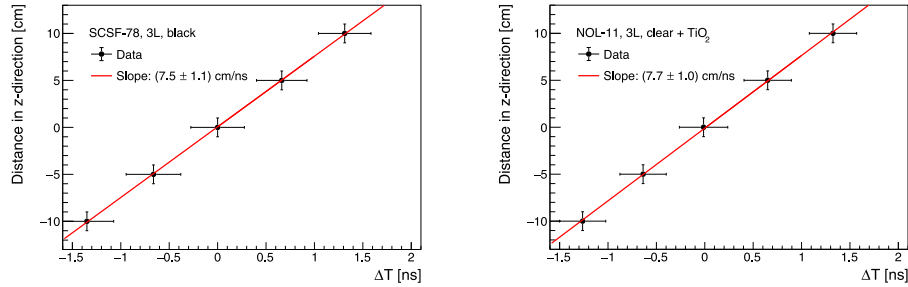


**Fig. 25.**  $\Delta T$  peak position vs beam impact point along the SciFi ribbon for a 3-layer SCSF-78 *black* (left) and for a 3-layer NOL-11 *clear* + 20%  $\text{TiO}_2$  fiber ribbon (right).

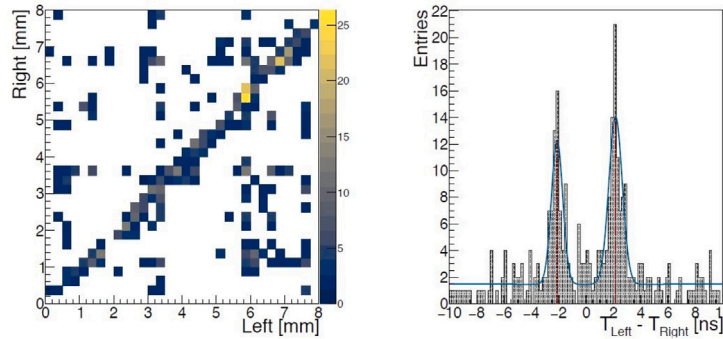


**Fig. 26.** (Left) Correlation between hits at both ribbon's ends generated by random discharges in one SiPM array. (right)  $T_{\text{left}} - T_{\text{right}}$  for these events.

could report separately the FWHM for the left and right sides of this distribution.

After subtraction of the trigger  $T_{\text{trigger}}$  time jitter  $\sigma_{\text{trigger}}$  of 80 ps, the time resolution  $\sigma_{MT}$  achievable with the 3-layer SCSF-78 *black* fiber ribbon is 245 ps, and it is 210 ps for a 4-layer SCSF-78 *black* fiber ribbon. Similarly,  $\sigma_{MT}$  is 235 ps for the 3-layer NOL-11 *clear* + 20%  $\text{TiO}_2$  fiber ribbon, and it is 200 ps for a 4-layer NOL-11 fiber

ribbon (Table 1). The 4-layer SCSF-78 fiber ribbons prepared with different adhesives show a similar timing performance. We conclude that different adhesives do not have a significant impact on the time resolution of our detectors. The effect of the shorter decay time of the NOL-11 fibers results in a reduced tail, which is visible when comparing the different  $MT$  distributions. However, the effect of increasing the number of staggered fiber layers is much more significant, which proves

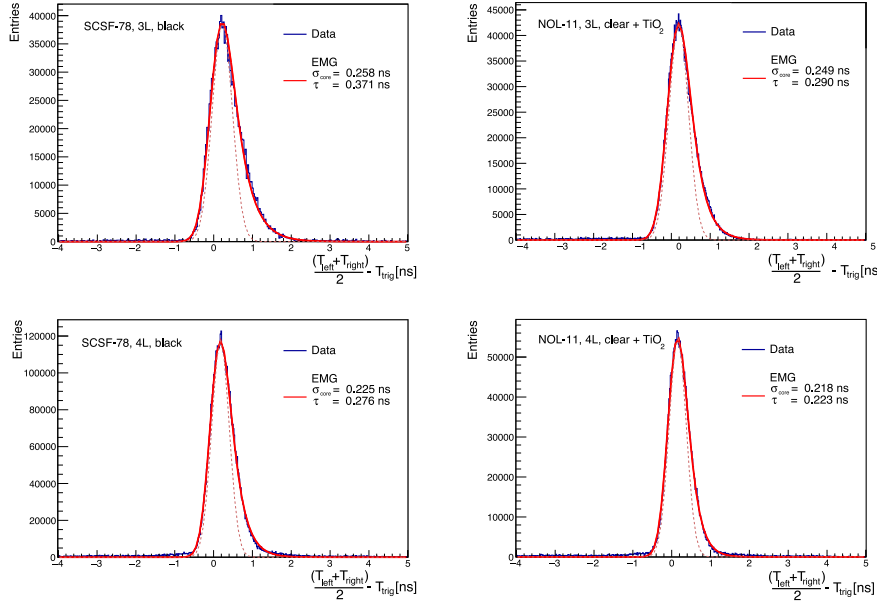


**Fig. 27.** Mean-Time  $MT$  distribution for different SciFi ribbons. The distributions are well described by the EMG distribution. The tails on the right of the peaks are driven by the fiber's decay time. The dashed line shows the Gaussian of the convolution with width  $\sigma_{\text{core}}$ .

**Table 1**

Timing performance of 3- and 4-layer SciFi ribbons made of different fibers.

Fiber type	# of layers	Adhesive	$\sigma_{AT}$ [ps]	$\sigma_{MT}$ [ps]	$\tau_{\text{EMG}}$ [ps]
SCSF-78	3	black	$456 \pm 9$	$245 \pm 6$	$371 \pm 12$
SCSF-78	4	black	$404 \pm 9$	$210 \pm 6$	$276 \pm 11$
SCSF-78	4	clear+20%TiO <sub>2</sub>	$409 \pm 9$	$218 \pm 6$	$275 \pm 10$
NOL-11	3	clear+20%TiO <sub>2</sub>	$409 \pm 9$	$235 \pm 6$	$290 \pm 11$
NOL-11	4	clear+20%TiO <sub>2</sub>	$395 \pm 9$	$200 \pm 6$	$223 \pm 11$

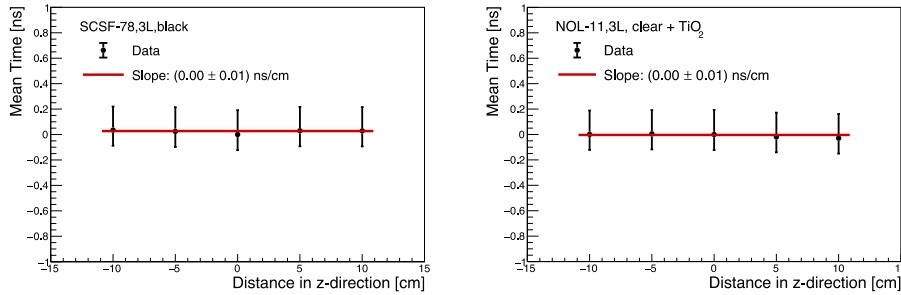


**Fig. 28.**  $MT$  as function of the impact point along the SciFi ribbon for a 3-layer SCSF-78 *black* fiber ribbon (left) and for a 3-layer NOL-11 *clear + 20% TiO<sub>2</sub>* fiber ribbon (right). The vertical error bars are taken at the FWHM of the  $MT$  distribution separately for the left and right sides of the  $MT$  distribution to reflect the shape of the distribution.

the importance of the light yield. The best timing performance of 200 ps has been achieved with a 4-layer NOL-11 SciFi ribbon.

Fig. 28 shows the peak values of the  $MT$  distribution for different beam impact points along the SciFi ribbon. Since the total distance traveled by the photons emitted in opposite hemispheres is constant (i.e. equal to the length of the ribbon) one can expect that the mean-time will not change along the ribbon and that it will be independent of the particle's impact point. Fig. 28 shows that indeed this is the case within our resolution, and that the width of the  $MT$  distribution does not change appreciably along the SciFi ribbon, as well. Therefore, the mean-time  $MT$  is a good observable for timing measurements.

## 9. Spatial resolution

The spatial resolution of the SciFi detector has been studied with a setup similar to the one illustrated in Fig. 7 at the CERN SPS using

a 150 GeV proton beam. At this energy the multiple scattering in the SciFi telescope is negligible in comparison to the tracking resolution of the telescope. Fig. 29 shows the distribution of residuals between the hit position measured in the third most downstream 4-layer SCSF-78 *clear* fiber detector and the hit position predicted by the tracks measured with the other three SciFi detectors. The residual distribution is fitted with a sum of two Gaussians with the same mean value to describe better the tails. The FWHM/2.35 of the residual distribution is 130  $\mu\text{m}$ . After subtracting the uncertainty on the track reconstruction of about 75  $\mu\text{m}$ , estimated by assuming that all four SciFi detectors in the telescope have the same resolution, a spatial resolution of about 100 ( $\pm 10$ )  $\mu\text{m}$  has been extracted. While this resolution is several times worse than the spatial resolution of the Mu3E tracking Si-pixel detectors, it will be essential for associating correctly a hit in the fiber detector to the tracks reconstructed in the Si-pixels.



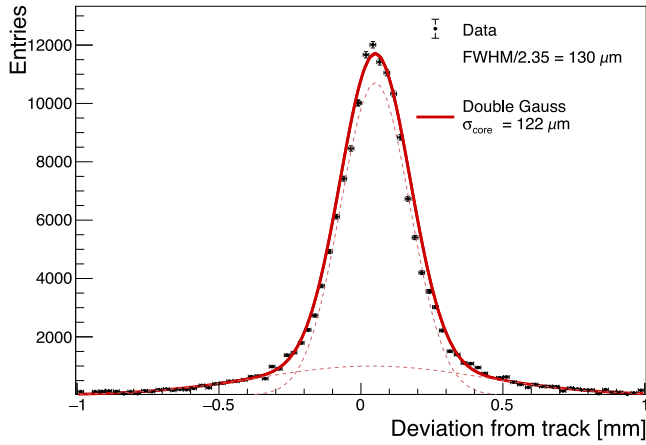


Fig. 29. Distribution of residuals between the clusters reconstructed in the DUT and the tracks reconstructed in the SciFi telescope. The residual distribution is fitted with a sum of two Gaussians to describe better the tails of the distribution. A spatial resolution of about 100  $\mu\text{m}$  is obtained after subtracting the track reconstruction uncertainty of 75  $\mu\text{m}$ .

## 10. Detection efficiency

The second most important feature of the SciFi detector is the detection efficiency. To associate a hit in the SciFi detector to a track reconstructed in the Mu3E Si-pixel tracking detectors (Fig. 1) and to extract the timing information, clusters are required to be identified at both sides of the fiber ribbons and to be matched in space and time. The *left* and *right* clusters are matched by requiring that they have at least one fiber in common, i.e. at least one matching channel in the two SiPM arrays at opposite ends. From the uncorrelated hit rate in Fig. 26 one can assess that almost all (i.e. > 99%) uncorrelated clusters from dark counts are rejected by this requirement. The clusters are matched in time by requiring that the time difference  $|\Delta T = T_{\text{left}} - T_{\text{right}}|$  is smaller than a predefined value, typically 3 or 5 times the width of the  $\Delta T$  distribution  $\sigma_{\Delta T}$ . In applying this selection one has to account for the drift of  $\Delta T$  along the fiber ribbon. Moreover, the time matching requirement rejects accidental combinations of clusters from track pileup at high rates.

### 10.1. HV bias dependence

Fig. 30 shows the single-sided cluster detection and matching efficiencies as a function of  $V_{\text{bias}}$ . The cluster selection requires at least one channel to pass the 1.5 ph.e. threshold with a  $5 \times \sigma_{\Delta T}$  timing cut for matched clusters. Since all channels of the SiPM array are operated at the same  $V_{\text{bias}}$ , and therefore at different  $V_{\text{ob}}$ , some inefficiencies at low over-bias voltages  $V_{\text{ob}}$  are observed. The single sided efficiency reaches a plateau around  $V_{\text{ob}} \approx 3$  V and remains relatively constant for higher values of  $V_{\text{bias}}$ . The cluster matching efficiency behaves similarly. Therefore, the operation voltage of the SiPM arrays has been set at  $V_{\text{bias}} = 55.5$  V (i.e.  $V_{\text{ob}} \geq 3$  V) for all SiPM arrays.

### 10.2. Threshold scans

Fig. 31 shows the single-sided cluster detection efficiency as a function of the hit selection threshold for a 3- and a 4-layer SCSF-78 black fiber ribbon. For clusters with a hit multiplicity  $\geq 1$  the detection efficiency does not drop much with increasing threshold. However, for clusters with a hit multiplicity  $\geq 2$  the efficiency drops rapidly, since most of the light signal is concentrated in one channel. This efficiency drop is less pronounced for a 4-layer SciFi ribbon. The *left* – *right* cluster matching efficiency, shown in Fig. 32 for different timing selections,

Table 2

Cluster matching efficiency in % for different thresholds, cluster multiplicities, and timing cuts for a 3-layer SCSF-78 black fiber ribbon.

thr.	Cluster	Single-sided	Matched clusters		
[ph.e.]	mult.	cluster	no $\Delta T$ cut	$ \Delta T  < 5\sigma_{\Delta T}$	$ \Delta T  < 3\sigma_{\Delta T}$
0.5	$\geq 2$	$97.5^{+0.3}_{-0.4}$	$97.5^{+0.3}_{-0.4}$	$96.8^{+0.4}_{-0.5}$	$93.6^{+0.5}_{-0.6}$
1.5	$\geq 1$	$99.4^{+0.1}_{-0.2}$	$99.4^{+0.1}_{-0.2}$	$98.3^{+0.2}_{-0.3}$	$95.5^{+0.4}_{-0.5}$
1.5	$\geq 2$	$84.3^{+0.6}_{-0.7}$	$84.3^{+0.6}_{-0.7}$	$83.9^{+0.7}_{-0.8}$	$80.3^{+0.7}_{-0.8}$
2.0	$\geq 1$	$98.4^{+0.2}_{-0.3}$	$98.4^{+0.2}_{-0.3}$	$97.3^{+0.4}_{-0.5}$	$94.7^{+0.5}_{-0.6}$
2.0	$\geq 2$	$72.7^{+1.1}_{-1.2}$	$72.6^{+1.1}_{-1.2}$	$72.3^{+1.1}_{-1.2}$	$71.1^{+0.2}_{-1.2}$
2.5	$\geq 1$	$96.6^{+0.9}_{-0.5}$	$96.5^{+0.4}_{-0.5}$	$95.5^{+0.4}_{-0.5}$	$93.0^{+0.5}_{-0.6}$
2.5	$\geq 2$	$66.9^{+0.9}_{-1.2}$	$66.5^{+0.8}_{-1.1}$	$66.1^{+1.1}_{-1.2}$	$64.3^{+0.9}_{-1.1}$

shows a similar behavior. The timing cut on  $|T_{\text{left}} - T_{\text{right}}|$  induces an additional drop in the efficiency, since this additional requirement removes events in the tails of the  $\Delta T$  distribution. These results are summarized in Table 2 for beam particles crossing perpendicularly the ribbons in the center.

Two different working points for the SciFi detector have thus been identified:

- require at least two contiguous channels to pass a threshold of 0.5 ph.e.; this removes most of the dark counts, since it is highly unlikely that two neighboring channels will discharge at the same time;
- require at least one channel to pass a threshold of 1.5 ph.e. (higher thresholds can also be applied); this suppresses the dark counts, since it is unlikely that they pass a higher threshold;

with a  $|\Delta T|$  timing selection of  $5 \times \sigma_{\Delta T}$ . More sophisticated clustering algorithms are possible, however here we tried to reproduce as much as possible the operation mode of the MuTriG ASIC, which allows for the setting of only one threshold per channel during data taking.

The detection efficiency of the SciFi detector assembled with clear epoxy containing  $\text{TiO}_2$  is few % higher. This is due to the 15% higher light yield of these ribbons. The NOL-11 fiber ribbons show a further increase of the detection efficiency for matched clusters, particularly for the stricter  $3 \times \sigma_{\Delta T}$  condition, because of the less pronounced tails in the  $\Delta T$  distribution.

### 10.3. Position scans

The uniformity of the cluster matching efficiency along the longitudinal (horizontal) and across the transverse (vertical) directions of the SciFi ribbons has been studied by evaluating the efficiencies for different beam impact points along the ribbon and in consecutive groups of 8 channels of the SiPM arrays (i.e. 2 mm), respectively. The resulting position-dependent efficiencies are shown in Fig. 33. The cluster matching efficiency is quite uniform along the SciFi ribbons despite the variation of the light yield along the ribbon.

### 10.4. Angular scans

Fig. 34 shows the cluster matching efficiency for different crossing angles for 3- and 4-layer SCSF-78 black fiber ribbons for different cluster selection criteria. As the crossing angle increases the cluster width broadens, and the detection efficiency increases. In Mu3E the particles will cross the SciFi ribbons at an average angle of  $27^\circ$ , which implies also a higher detection efficiency for Mu3E as reported in Table 2. For a  $60^\circ$  incident angle the effective thickness of the SciFi ribbon doubles, and the detection efficiency is above 99% regardless of the selection criteria.

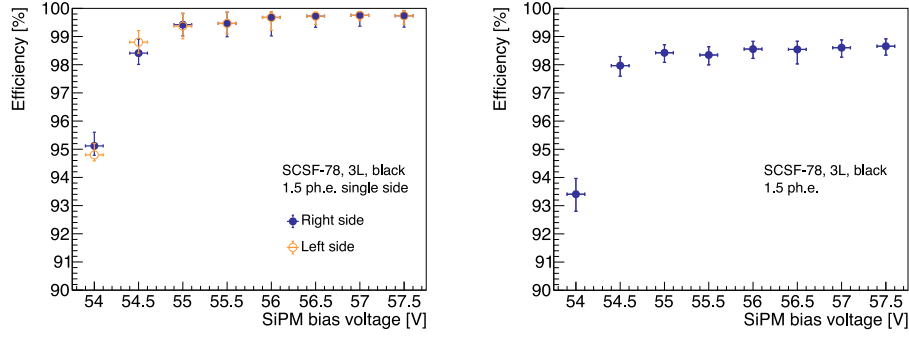


**Fig. 30.** Single sided cluster detection efficiency (left) and cluster matching efficiency (right) vs  $V_{\text{bias}}$  for a 3-layer SCSF-78 *black* fiber ribbon. A threshold of 1.5 ph.e. is applied to the hit validation and a timing cut of  $5 \times \sigma_{\Delta T}$  is applied to select matching clusters.

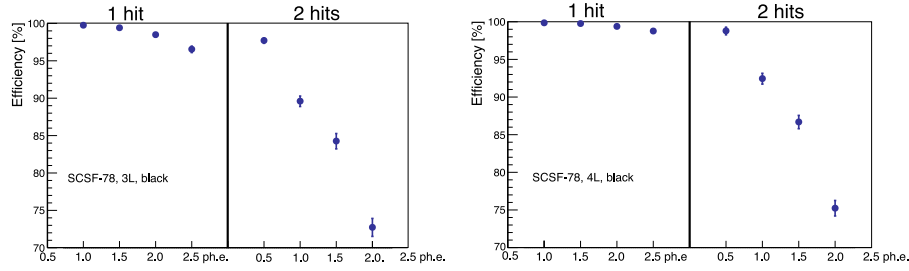


**Fig. 31.** Single-sided cluster detection efficiency vs threshold for a 3-layer (left) and a 4-layer (right) SCSF-78 *black* fiber ribbon for cluster multiplicities  $\geq 1$  and  $\geq 2$ .

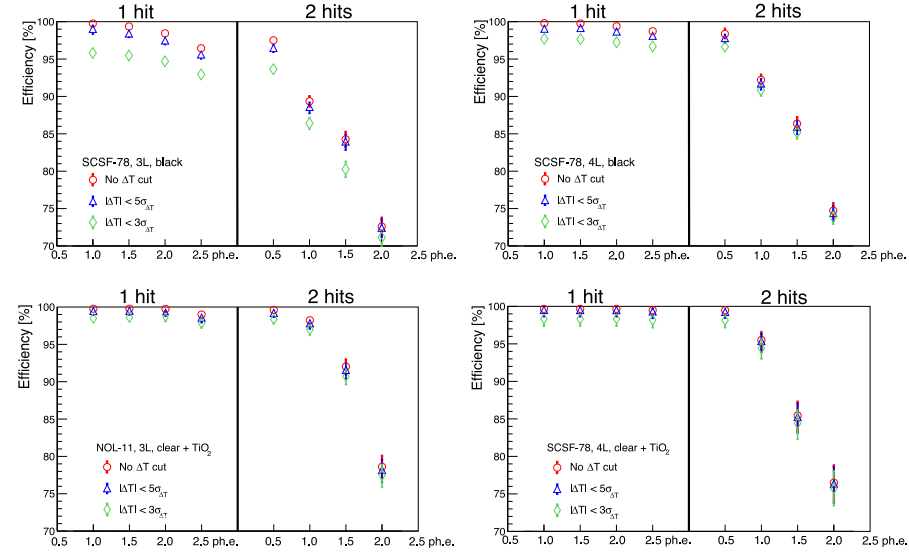


**Fig. 32.** Cluster matching efficiency vs threshold for  $\geq 1$ -hit and  $\geq 2$ -hit clusters for different  $\Delta T$  selections (no  $\Delta T$  cut,  $5 \times \sigma_{\Delta T}$ , and  $3 \times \sigma_{\Delta T}$ ).

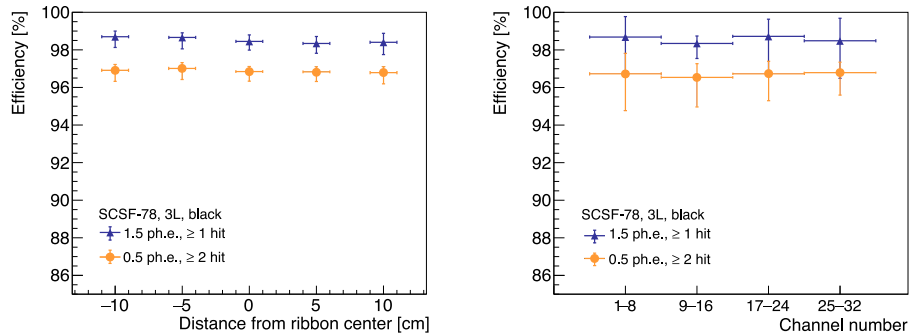


**Fig. 33.** Cluster matching efficiency vs beam impact point along (left) and across (right) the SciFi ribbon for a 3-layer SCSF-78 *black* fiber ribbon. The  $5 \times \sigma_{\Delta T}$  selection is applied.

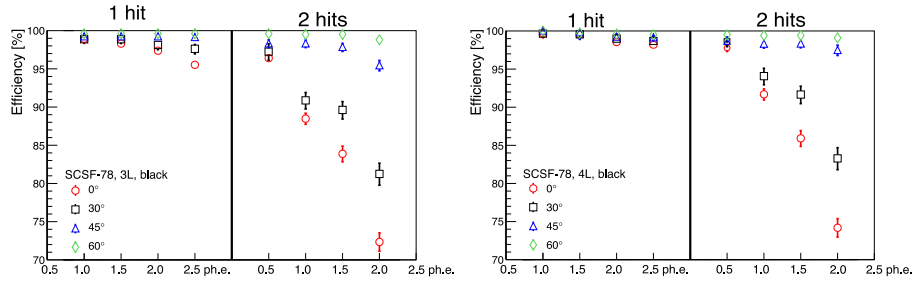


Fig. 34. Cluster matching efficiency vs crossing angle for a 3-layer (left) and 4-layer (right) SCSF-78 black fiber ribbon. The  $5 \times \sigma_{AT}$  selection is applied.

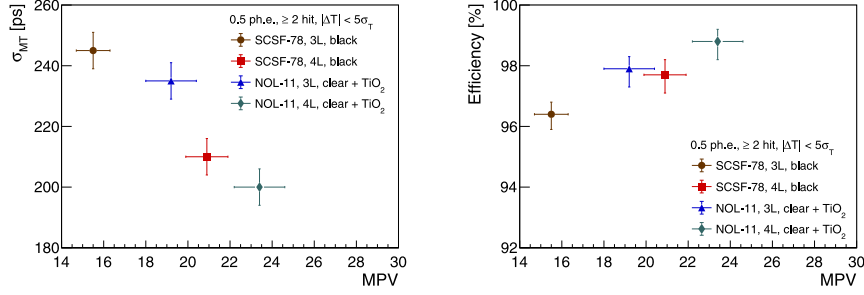


Fig. 35. Mean-time resolution  $\sigma_{MT}$  (left) and detection efficiency (right) vs light yield  $\langle n_{ph.e.} \rangle$ (MPV) for different SciFi ribbons. The 0.5 ph.e. threshold is used to select hits and a  $5 \times \Delta T$  cut is applied to select matched clusters with hit multiplicity  $\geq 2$  (w.p. 1).

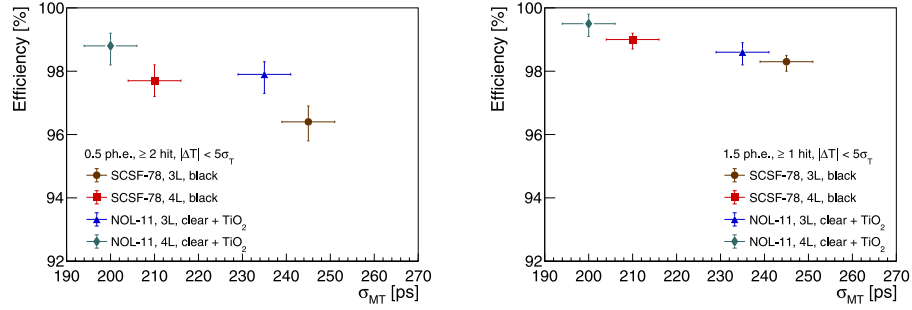


Fig. 36. Detection efficiency vs mean-time resolution  $\sigma_{MT}$  for different SciFi ribbons for two working points of the SciFi detector: (left) w.p. 1 (right) w.p. 2.

## 11. Performance of the SciFi detector

The most important features of the SciFi detector for Mu3E are the time resolution and the detection efficiency. Fig. 35 compares the mean-time resolution  $\sigma_{MT}$  and the detection efficiency with the light yield  $\langle n_{ph.e.} \rangle$  for the SciFi ribbons made of 3 and 4 staggered fiber layers with SCSF-78 and NOL-11 fibers. Fig. 36 shows the mean-time resolution  $\sigma_{MT}$  vs efficiency for these ribbons for the two working points of the SciFi detector introduced above (w.p. 1: threshold  $\geq 0.5$  ph.e. &  $n_{hits} \geq 2$  and w.p. 2: threshold  $\geq 1.5$  ph.e. &  $n_{hits} \geq 1$ ). The results are summarized in Table 3.

The best mean-time resolution  $\sigma_{MT}$  of 200 ps has been achieved with 4-layer SciFi ribbons made with NOL-11 fibers, while  $\sigma_{MT}$  for 3-layer SCSF-78 fiber ribbons is of 245 ps. Despite the much shorter decay time of the spectral shifter of 1.1 ns for the NOL-11 fibers compared to the decay time of 2.8 ns for the SCSF-78 fibers, the improvement on  $\sigma_{MT}$  is of only about 5%, while the tail in the MT distribution is reduced by 20%. The addition of one fiber layer leads to a larger improvement on  $\sigma_{MT}$  of about 15%, which shows the importance of the light yield for achieving a good time resolution.

The light yield of the SCSF-78 and NOL-11 fibers is comparable. The addition of  $TiO_2$  to the clear epoxy increases the light yield by about 15%, because a larger fraction of scintillation photons undergo diffused reflection at the fiber's outer skin, while the black epoxy reduces the

Table 3

Performance of different SciFi ribbons (different fiber types, number of fiber layers, and adhesive) for two different working points (w.p. 1  $\equiv thr \geq 0.5$  ph.e. &  $n_{hits} \geq 2$ ; w.p. 2  $\equiv thr \geq 1.5$  ph.e. &  $n_{hits} \geq 1$ ). The light yield and time resolution are reported for the w.p. 1.

Ribbon type	$\langle n_{ph.e.} \rangle$	$\sigma_{AT}$ [ps]	$\sigma_{MT}$ [ps]	eff. [%]	
				w.p. 1	w.p. 2
SCSF-78 3L black	$15.5 \pm 0.8$	$456 \pm 9$	$245 \pm 6$	$96.8^{+0.4}_{-0.5}$	$98.3^{+0.2}_{-0.3}$
SCSF-78 4L black	$20.9 \pm 1.0$	$404 \pm 9$	$210 \pm 6$	$97.7^{+0.5}_{-0.6}$	$99.0^{+0.2}_{-0.3}$
SCSF-78 4L $TiO_2$	$23.6 \pm 1.4$	$409 \pm 9$	$218 \pm 6$	$98.0^{+0.6}_{-0.9}$	$99.2^{+0.4}_{-0.6}$
NOL-11 3L $TiO_2$	$19.2 \pm 1.2$	$409 \pm 9$	$235 \pm 6$	$97.9^{+0.4}_{-0.6}$	$98.6^{+0.3}_{-0.4}$
NOL-11 4L $TiO_2$	$23.4 \pm 1.2$	$395 \pm 9$	$200 \pm 6$	$98.8^{+0.4}_{-0.6}$	$99.5^{+0.3}_{-0.4}$

cluster width (and consequently the optical cross-talk) by about 20% at low thresholds of 0.5 ph.e. The different adhesives do not have a significant impact on the time resolution of the SciFi detector, but impact the detection efficiency.

The detection efficiency is around 97% for a minimum cluster multiplicity of 2 passing the 0.5 ph.e. hit selection threshold (w.p. 1), and it is around 98% for clusters formed with at least one hit passing the 1.5 ph.e. threshold (w.p. 2). The  $5 \times \sigma_{AT}$  time cluster matching selection has always been applied. With a time cut of  $3 \times \sigma_{AT}$  the detection

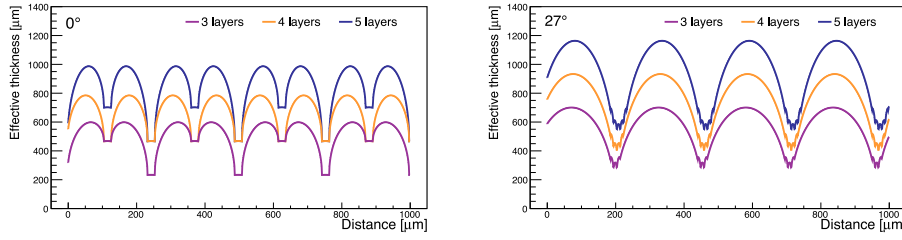


Fig. 37. Effective thickness of the active fiber material traversed by particles crossing the SciFi ribbon at and angle of  $0^\circ$  (left) and  $27^\circ$  (right) as a function of the impact point across the ribbon for different numbers of staggered fiber layers.

efficiency drops by about 3%. Adding one fiber layer increases the detection efficiency by 1% to 3% depending on the selection of the working point. As the thickness of the SciFi ribbons increases, the light yield increases almost linearly with the number of staggered fiber layers, and the higher light yield leads to a higher detection efficiency of the detector. As the particle's incident angle increases, the efficiency increases reaching virtually 100% for an angle of  $60^\circ$  because more SiPM array channels satisfy the hit selection criteria. The detection efficiency of the SciFi detector assembled with clear epoxy containing  $\text{TiO}_2$  is few % higher thanks to the 15% higher light yield of these ribbons. The NOL-11 fiber ribbons show a further increase of the detection efficiency, particularly for the stricter  $3 \times \sigma_{\Delta T}$  cluster matching condition. The final choice on the working point, i.e. how to validate hits and clusters, will be based on the behavior of the detector in the Mu3E experiment and the DCR of the SiPMs.

The response of the detector (time resolution, detection efficiency), within our resolution, is uniform. In particular, the mean-time does not depend on the hit position in the SciFi detector, confirming that  $MT$  is a good observable for time measurements. Finally, the speed of light propagation of scintillation photons in the fibers is half the speed of light in vacuum (i.e.  $v_{\text{fiber}} \sim 0.5 \times c$ ).

Some of the features of the SciFi detector can be understood from the structure of the fiber ribbons. Fig. 37 shows the effective thickness of the active fiber material traversed by particles crossing the ribbons at an angle of  $0^\circ$  and  $27^\circ$  as a function of the impact point across the ribbon. An effective diameter of  $230 \mu\text{m}$  for the fibers, which excludes the cladding, has been assumed. A *resonance* effect, emphasizing the structure of the ribbon, occurs around  $30^\circ$  (incidentally this angle is close to the average crossing angle in Mu3E of  $27^\circ$ ). The non-uniform thickness of the traversed active material leads to events with a low number of detected photons (Fig. 18), which in turn limits the detection efficiency and generates large fluctuations in the time measurements.

## 12. Outlook

In conclusion, we have developed a very thin scintillating fiber detector with a thickness  $< 0.2\%$  of a radiation length  $X_0$ . Not only does the Mu3E timing detector have to be extremely thin, which results in small primary signal amplitudes, but it also has only very limited physical space at its disposal (at the level of just a few centimeters for the front-end electronics). The SciFi detector is made of 3 layers of  $250 \mu\text{m}$  diameter round scintillating fibers, type SCSF-78 from Kuraray, read out with multi-channel SiPM arrays at both ends. The detector has a time resolution of around 250 ps, detection efficiency of about 97% when requiring coincident signals on both sides of the SciFi ribbon, and spatial resolution of  $\sim 100 \mu\text{m}$ . The combination of the SciFi and of the Si-pixel tracking detectors, with a vertex resolution better than  $300 \mu\text{m}$ , will allow for a full 4-dimensional reconstruction of the three body muon  $\mu^+ \rightarrow e^+e^-e^+$  decay at a precision sufficient to reach a sensitivity at the level of  $10^{-15}$  (at 95% CL) within two years of data taking with a muon beam intensity of  $10^8$  muons/s.

The SciFi technology can be used in a variety of applications requiring very good time and spatial resolutions, and high detection

efficiency with a very low material budget, capable of operating at high rates. Moreover, the use of SiPMs allows to operate these detectors in magnetic fields. To obtain a very good timing resolution, the chosen sensitive material has to feature fast rise time and high Signal-to-Noise ratio (i.e. a large primary signal amplitude and high light yield). The shorter decay time of the newest NOL-11 scintillating fibers, however, does not show a major advantage over the more conventional SCSF-78 fibers for this small size detector. The stringent Mu3E requirements impose the use of SciFi ribbons consisting of only 3 staggered fiber layers. This limits the light yield of the detector, which in turn has an impact on the time resolution and the detection efficiency. Otherwise SciFi ribbons with more staggered fiber layers would significantly increase the light yield and improve the overall performance of the detector, but at the cost of an increased material budget.

In principle, a timing resolution much better than a few 100 ps can be reached by a variety of other detector types, such as crystal scintillators (e.g. LYSO crystals), which feature intrinsic signal rise times of few 10 ps and much larger primary signal amplitudes (some 30k photons/MeV). However, the real challenge to be met in Mu3E is the requirement that the timing device has to detect electrons from muon decays of very low momenta of order 10 – 50 MeV without affecting their momentum through multiple scattering in order not to deteriorate the high tracking precision of the Si-pixel detectors. That rules out crystal scintillators which are by far too thick and bulky. Therefore, our chosen solution with thin scintillating fibers and 3 layers of staggered scintillating fibers has been shown to be a valid one that satisfies the extremely tight and challenging Mu3E requirements.

The intrinsic limit of this scintillating fiber detector comes from the sustainable rates, which will be exceeded in Phase II of the Mu3E experiment with muon rates above  $10^9$  muons/s. We anticipate that other, mostly silicon-based technologies, which are capable of both high tracking precision and very good timing resolutions at these very high rates, will become available in the future. Such new detectors, as e.g. very thin HV-MAPS Si-pixel detectors with a time resolution  $< 100$  ps, are in development at various laboratories.

## Declaration of competing interest

The authors declare that they have no known competing financial interests or personal relationships that could have appeared to influence the work reported in this paper.

## Data availability

The *metadata* repository for the measurements presented in this work can be found at <https://doi.org/10.16907/10be2b23-4783-4c5e-a17f-7ffdf4eb6527>. Data can also be made available on request.

## Acknowledgments

We would like to thank the technical staff at our institutes (F. Cadoux, Y. Favre, S. Debieux) for their help in developing the tools, mechanics, and electronics for this work. We thank the Paul Scherrer



Institut as host laboratory and for the technical support. We warmly thank our Mu3e collaborators for many interesting discussions. The Swiss institutes acknowledge the funding support from the Swiss National Science Foundation grants no. 200021\_165568, 200020\_182031, 200021\_172519, and 200020\_100642. The University of Geneva team gratefully acknowledges support from the Ernest Boninchi Foundation in Geneva. This work was also supported by ETH Research Grant ETH-11 13-1.

## References

- [1] Mu3e Collaboration, A. Blondel, et al., Research Proposal for an Experiment to Search for the Decay  $\mu \rightarrow eee$ , [arXiv:1301.6113](https://arxiv.org/abs/1301.6113).
- [2] Mu3e Collaboration, K. Arndt, Technical design of the phase I Mu3e experiment, *Nucl. Instrum. Methods A* 1014 (2021) 165679.
- [3] Hamamatsu Photonics, <https://www.hamamatsu.com/us/en/product/optical-sensors/mppe/mppe-array/S13552.html>.
- [4] R.C. Ruchti, The use of scintillating fibers for charged-particle tracking, *Annu. Rev. Nucl. Part. S.* 46 (1996) 281.
- [5] P. von Doetinchem, et al., Positron electron balloon spectrometer, *Nucl. Instrum. Methods A* 581 (2007) 151.
- [6] B. Beischer, et al., A high-resolution scintillating fiber tracker with silicon photomultiplier array readout, *Nucl. Instrum. Methods A* 622 (2010) 542.
- [7] LHCb Collab, LHCb Upgrade I, [arXiv:2305.10515](https://arxiv.org/abs/2305.10515).
- [8] W. Shen, et al., A silicon photomultiplier readout ASIC for time-of-flight application using a new time-of-recovery method, *IEEE Trans. Nucl. Sci.* 65 (2018) 1196.
- [9] Kuraray Co., <http://kuraraypsf.jp/index.html>.
- [10] O. Borshchev, et al., Development of a new class of scintillating fibres with very short decay time and high light yield, *J. Instrum.* 12 (2017) P05013.
- [11] Saint-Gobain Crystals, <https://www.crystals.saint-gobain.com/products/scintillating-fiber>.
- [12] A. Bravar, Y. Demets, Timing properties of blue-emitting scintillating fibers, *J. Instrum.* 17 (2022) P12020.
- [13] O. Girard, et al., Characterization of silicon photomultipliers based on statistical analysis of pulse-shape and time distributions, [arXiv:1808.05775](https://arxiv.org/abs/1808.05775).
- [14] S. Ritt, R. Dinapoli, U. Hartmann application of the DRS chip for fast waveform digitizing, *Nucl. Instrum. Methods A* 623 (2010) 486.
- [15] A. Damyanova, Development of the Scintillating Fiber Detector for Timing Measurements in the Mu3e Experiment (Ph.D. thesis), University of Geneva, 2019.